

Spectroscopy of superconducting charge qubits coupled by a Josephson inductance

T. Yamamoto,^{1,2} M. Watanabe,² J. Q. You,^{2,3} Yu. A. Pashkin,^{1,2,*}
O. Astafiev,^{1,2} Y. Nakamura,^{1,2} F. Nori,^{2,4} and J. S. Tsai^{1,2}

¹*NEC Nano Electronics Research Laboratories, Tsukuba, Ibaraki 305-8501, Japan*

²*Frontier Research System, The Institute of Physical and Chemical Research (RIKEN), Wako-shi, Saitama 351-0198, Japan*

³*Department of Physics and Surface Physics Laboratory (National Key Laboratory), Fudan University, Shanghai 200433, China*

⁴*Center for Theoretical Physics, Physics Department, Center for the Study of Complex Systems,
The University of Michigan, Ann Arbor, Michigan 48109-1040, USA*

(Dated: November 28, 2007)

We have designed and experimentally implemented a circuit of inductively-coupled superconducting charge qubits, where a Josephson junction is used as an inductance, and the coupling between the qubits is controlled by an applied magnetic flux. Spectroscopic measurements on the circuit are in good agreement with theoretical calculations. We observed anticrossings which originate from the coupling between the qubit and the plasma mode of the Josephson junction. Moreover, the size of the anticrossing depends on the external magnetic flux, which demonstrates the controllability of the coupling.

PACS numbers: 85.25.Cp, 03.67.Lx

I. INTRODUCTION

Recently, mesoscopic superconducting circuits have been extensively studied because of their potential applications for quantum information processing.^{1,2,3,4} Since the first demonstration⁵ of coherent oscillations in a superconducting quantum bit (qubit), the quality of single qubits has increased rapidly. In particular, the coherence time of a single qubit has improved significantly.⁶ The mechanisms of decoherence have been intensively studied^{7,8,9,10,11}, and it is commonly accepted that in order to obtain longer coherence times, charge and flux qubits must be biased at the optimal point, where the qubit is insensitive, to first order, to fluctuations of the bias parameters.

There has also been much progress on multiple-qubit systems.^{12,13,14,15,16,17,18,19} One of the recent important topics in this field is how to best achieve controllable couplings between qubits,^{20,21,22,23,24,25} and there are many theoretical proposals on controllable coupling schemes.^{26,27,28,29,30,31,32,33,34,35,36,37,38,39,40,41,42,43} Although it is advantageous that two-qubit gate operations can be performed at the optimal point, some of the theoretical proposals cannot be used at the optimal point. A solution to this problem was proposed in Ref. 32, who employed a technique similar to the one known as double-resonance in nuclear magnetic resonance.⁴⁴ This and other ideas^{30,42} were further developed to become a so-called parametric coupling,^{35,37,43} and it was recently demonstrated in time-domain experiments.²³

An alternative way to couple qubits at the optimal point is to use a “longitudinal” coupling, namely, an inductive coupling for charge qubits or a capacitive coupling for flux qubits.^{27,28,31,33,45,46} In this case, the coupling term directly affects the energy levels at the optimal point.

Here we report an experimental study of inductively-coupled charge qubits based on the theoretical study in Refs. 27 and 28. In this approach, an extra Josephson junction provides an inductive coupling between the qubits. This inductive coupling, controlled by a magnetic flux bias, is quite different from the usual capacitive coupling between charge qubits. The inductive coupling term and the single-qubit term in the Hamiltonian of the system at the charge degeneracy point commute with each other, which means that the eigenstates there are the tensor products of the uncoupled qubits. Thus, the system, when initially prepared in one of the eigenstates, does not evolve to an entangled state, which makes the sequence of qubit operations for the computation simpler. Moreover, the strength of the coupling can be controlled without changing the gate-induced charge. Thus, the system can always stay at the charge degeneracy point during qubit manipulations.

Another important feature of this approach is its scalability. Although here we study a circuit consisting of two qubits coupled by a single Josephson junction, more qubits, in principle, can be coupled to the same Josephson junction, as discussed in Ref. 27. Alternatively, one can make a one-dimensional chain of a qubit and a single Josephson junction, as discussed in Refs. 31 and 33. The coupling between neighboring qubits can be controlled either by a magnetic flux bias applied to them or a current bias applied to the single Josephson junction between them.

II. EXPERIMENT

A. Circuit design

Figure 1a represents a diagram of the circuit. This circuit consists of two charge qubits (left and right) and a single Josephson junction shunted by a capacitance C_s (center). The single Josephson junction is shared by two loops of the corresponding qubit (a split Cooper-pair box), where two nominally-identical Josephson junctions are attached to a superconducting small island (filled dot). The single Josephson junction serves as an inductor which couples the circulating currents of the two qubits. Because the magnitude of the circulating current depends on the flux penetrating the loop, we can control the strength of the coupling between the qubits by an external magnetic field.

The Hamiltonian of this circuit, a generalization from the one for the single qubit with a large Josephson junction,⁴⁷ is given by

$$H = \sum_{i=1}^2 E_{ci}(n_i - n_{gi})^2 - 2E_{J1} \cos \phi_{p1} \cos\left(\pi f + \frac{\phi_0}{2}\right) - 2E_{J2} \cos \phi_{p2} \cos\left(\pi f - \frac{\phi_0}{2}\right) + E_{c0}\left(n_0 + \frac{n_{g1} + n_{g2}}{2}\right)^2 - E_{J0} \cos \phi_0. \quad (1)$$

Here (for $i = 1, 2$), $E_{ci} = (2e)^2/4C_i$ is the Cooper-pair charging energy of the Cooper-pair box (we assume $C_{gi} \ll C_i$), n_i is the number of excess Cooper pairs in the island, $n_{gi} = C_{gi}V_{gi}/2e$ is the normalized gate-induced charge on the island, E_{Ji} is the Josephson energy of each junction of the split Cooper-pair box, and ϕ_{pi} ($= \phi_{Ai} - \phi_{Bi}$) is the total phase drop across the two junctions of the split Cooper-pair box. The charging energy and the Josephson energy of the coupling junction are denoted by $E_{c0} = (2e)^2/2[C_0 + C_s + (C_1 + C_2)/2]$ and E_{J0} , respectively. The phase drop across the coupling junction is denoted by ϕ_0 , and n_0 is its conjugate variable. We assume equal magnetic flux in the two loops, and define the relative flux bias $f = \Phi_{\text{ex}}/\Phi_0$, where Φ_{ex} is the magnetic flux in each loop and Φ_0 is the flux quantum.

When the conditions $E_{J1,2} \ll E_{J0}$ and $E_{c0} \ll E_{J0}$ are satisfied, the above Hamiltonian is simplified to the following effective Hamiltonian for two coupled qubits, based on the charge state of each Cooper-pair box,²⁸

$$H_{\text{eff}} = -\frac{1}{2} \sum_{i=1}^2 \left[E_{ci}(1 - 2n_{gi}) \sigma_{zi} + 2E_{Ji}^* \cos(\pi f) \sigma_{xi} \right] + \chi \sigma_{x1} \sigma_{x2}. \quad (2)$$

Here

$$\chi \equiv \chi(f) = \frac{E_{J1}E_{J2}}{4E_{J0}} \sin^2(\pi f) \quad (3)$$

is the strength of the interbit coupling, and

$$E_{Ji}^* = E_{Ji} \left[1 - \frac{3}{32E_{J0}^2} (E_{Ji}^2 - E_{Jj}^2) \sin^2(\pi f) \right], \quad (4)$$

where $i, j = 1, 2$ ($i \neq j$). Note the difference in the sign of the coupling term in Eq. (2) from that in Ref. 28. This is because of the different circuit geometry. Note also that E_{Ji}^* is almost equal to E_{Ji} because $E_{Ji} \ll E_{J0}$ and $E_{Ji} \sim E_{Jj}$. The advantage of this scheme is that the Hamiltonian [Eq. (2)] at the charge degeneracy point $n_{g1} = n_{g2} = 0.5$ consists of *only* σ_x terms, and the eigenstates can be used as two-qubit bases because they are tensor products of uncoupled qubits. Moreover, we do *not* need to change n_{gi} when we want to change the strength of the coupling, meaning that we can stay at the charge degeneracy point for *both* qubits during the qubit manipulations, which is preferable from the viewpoint of preserving the coherence of the qubits.⁶

Now let us consider the range of device parameters to realize this effective Hamiltonian. In principle, a larger E_{J0} is desirable for this approach. However, in order to observe the effect of the coupling within the limited coherence time T_2 , we cannot make E_{J0} too large because the coupling coefficient χ is inversely proportional to E_{J0} . More quantitatively, it is required that

$$\chi_0 \equiv \frac{E_{J1}E_{J2}}{4E_{J0}} > \frac{\hbar}{T_2}. \quad (5)$$

Because the qubit parameters in this study are quite similar to those of our previous experiments,^{5,12,14} T_2 is expected to be of the same order, namely ~ 1 ns at the charge degeneracy point. The qubit Josephson energy $2E_{Ji}/\hbar$ is typically

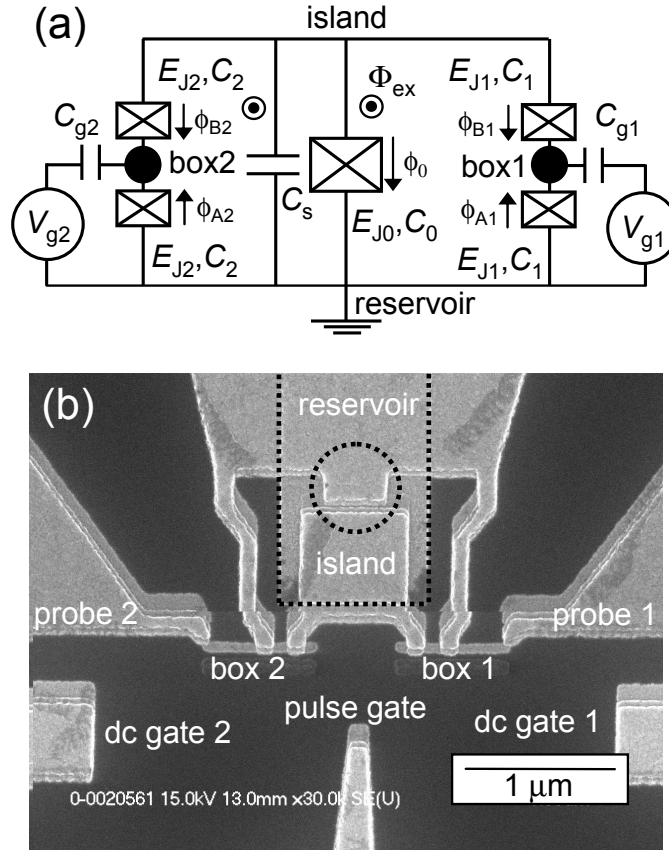


FIG. 1: (a) Schematic circuit diagram of inductively-coupled charge qubits. Rectangles with an X inside denote Josephson junctions with corresponding Josephson energy E_{Ji} and junction capacitance C_i . The arrow near each junction denotes the chosen direction for the positive phase drop across the corresponding junction. (b) A scanning electron micrograph of a sample. A rectangular-shape electrode indicated by the dotted rectangles is connected to the reservoir and forms a shunt capacitance with the large island in the middle of the picture. The Josephson junction for the qubit coupling, inside the dotted circle, links the reservoir and the large island. Two probe electrodes and a pulse-gate electrode are shown in (b), but not in (a).

~ 10 GHz, meaning that E_{J0}/E_{Ji} can be of order unity at maximum. Consequently, we designed E_{J0}/E_{Ji} to be about 4 in the present study. Because of this limitation on the size of the coupling junction, the junction capacitance C_0 alone is not large enough to safely meet the requirement $E_{c0} \ll E_{J0}$. To overcome this problem, we shunted the junction by an additional capacitance C_s . However, this capacitance cannot be arbitrarily large, because we do not want to excite the plasma mode of the coupling junction. Therefore, here we require the condition $E_{Ji} \ll h\nu_p$, where $\nu_p = \sqrt{2E_{J0}E_{c0}}/h$ is the plasma frequency of the coupling junction.

B. Sample fabrication

Figure 1b shows a scanning-electron-microscope (SEM) image of the sample. First, we prepared gold pads with a ground plane, and a coplanar waveguide on an oxidized Si substrate by a photo-lithography process. A 300-nm thick SiN_x grown by plasma chemical vapor deposition at a temperature of 250°C was used as an insulator between the gold pads and the ground plane.

After this photo-lithography process, the device was fabricated by a two-step electron-beam-lithography process using a trilayer resist [poly-methyl-methacrylate (PMMA)/Ge/poly-(methylmethacrylate-methacrylic acid) P(MMA-MAA), 50/20/200 nm thick]. In the first e-beam step, a rectangular-shape 30-nm thick Al electrode was evaporated after the e-beam pattern was transferred to the Ge mask and the bottom layer resist P(MMA-MAA) was etched by oxygen plasma. It is shown by the dotted rectangle in the top part of Fig. 1b and it was connected to the same gold pad (not shown) as the one to which the reservoir electrode was connected. Then the sample was brought out of the vacuum and a trilayer resist was again prepared. The surface of the Al electrode prepared in the first deposition was strongly oxidized during the following etching process (same as the one in the first step).

Then, the coupled-qubit circuit was fabricated by a three-angle evaporation of Al (10/30/40 nm thick). After the evaporation of the first layer of Al, 70 mTorr oxygen was introduced into the chamber for 4 minutes typically, which forms tunnel barriers for the Cooper-pair boxes and the Josephson junction for the coupling (coupling junction). As shown by the dotted circle in Fig. 1b, the coupling junction was formed between the reservoir and the large island in the middle of the figure. The large island was overlapping with the rectangular-shape electrode underneath, forming a shunt capacitance for the coupling junction. From independent measurements of the current-voltage (I - V) characteristics of similar single electron transistors, the junction capacitance per area was estimated to be $13 \text{ fF}/\mu\text{m}^2$. The overlapping area between the large island and the rectangular-shape electrode was estimated from the SEM image to be $0.71 \times 0.73 \mu\text{m}^2$, which gives a capacitance of 6.8 fF.

Besides those shown in Fig. 1a, there are probe electrodes for qubit readout and a pulse gate for qubit control. The probe electrode is attached to each box via a high-resistive tunnel junction (typically $30 \text{ M}\Omega$), which was formed by introducing 1 atm oxygen into the chamber for 10 minutes after the evaporation of a second layer of Al. A continuous microwave or a fast voltage pulse was applied to the pulse gate electrode, which is coupled almost equally to the two boxes.

C. Measurement setup

All the measurements were performed using a dilution refrigerator at a base temperature of about 40 mK. DC signals were measured with a battery-powered preamplifier box. Bias voltages were supplied through resistive dividers and RC filters in the box. For the probe bias, a voltage-feedback loop was also used. DC signal lines were low-pass filtered by commercial LC π -filters at the top of the cryostat, home-made RC filters at each stage of the dilution refrigerator, and the cables themselves (lossy CuNi coaxial cables). No DC signal lines were connected to the ground at low temperatures. For the transmission of high-frequency continuous microwaves or fast voltage pulses, silver-plated BeCu(inner)/SUS(outer) coaxial cables were used from room temperature to 4.2 K and Nb coaxial cables were used from 4.2 K to the base temperature. A 20-dB fixed attenuator was used at 4.2 K. A magnetic field was applied homogeneously to the device by a superconducting solenoid installed in the liquid helium bath.

D. Sample characterization

To characterize the device parameters, we first measured the I - V characteristics of each qubit. We obtained the charging energy of each qubit from the slope of the Coulomb diamonds.

Next we measured the field dependence of the two probe currents. Figure 2(a) shows the two probe currents of one sample (sample A) as a function of the external magnetic field. Two probes were biased at $720 \mu\text{V}$, so that the Josephson quasiparticle (JQP) cycle⁴⁸ was activated. The DC gate voltages were adjusted so that each qubit was operated at the slope of the JQP peaks. As seen in the figure, the two currents are modulated by the applied magnetic field, indicating that the effective Josephson energy of each qubit is controllable due to the SQUID geometry. The modulation periods for the two currents are almost the same, as expected from nominally-equal loop sizes.

Finally, we measured the coherent oscillations of each qubit to estimate the Josephson energy. Figure 2(b) shows coherent oscillations of the same sample at the flux bias $f=0.00$. Two probe currents are plotted there as a function of the duration time of a non-adiabatic voltage pulse applied to the gate electrode.^{5,12,14} The measurements were done in such a way that while one qubit was oscillating at its charge degeneracy point, the other qubit was in the Coulomb blockade regime. We measured the coherent oscillations under different flux biases, and confirmed that the oscillation frequency showed a cosine dependence on f , from which we determined E_{Ji} .

We fabricated samples with different E_{Ji}/E_{Ci} ratios of the qubit and different E_{J0}/E_{Ji} ratios. We also fabricated a reference sample which had the same circuit geometry, but did not have a coupling junction. We summarize the parameters of the measured samples in Table I. The parameters for the coupling junction were estimated based on the junction-area measurements by taking scanning electron micrographs.

E. Spectroscopic measurements

To probe the excited states of our coupled-qubit system, we carried out spectroscopic measurements using a continuous microwave. All the samples listed in Table I showed qualitatively the same behavior except for sample E, which had no coupling junction. Here we focus on sample A.

Figure 3 shows an example of the spectroscopic measurements. In the figure, the current through probe 2 (I_2) is plotted as a function of n_{g2} with (solid line) and without (dotted line) microwave irradiation. Under microwave

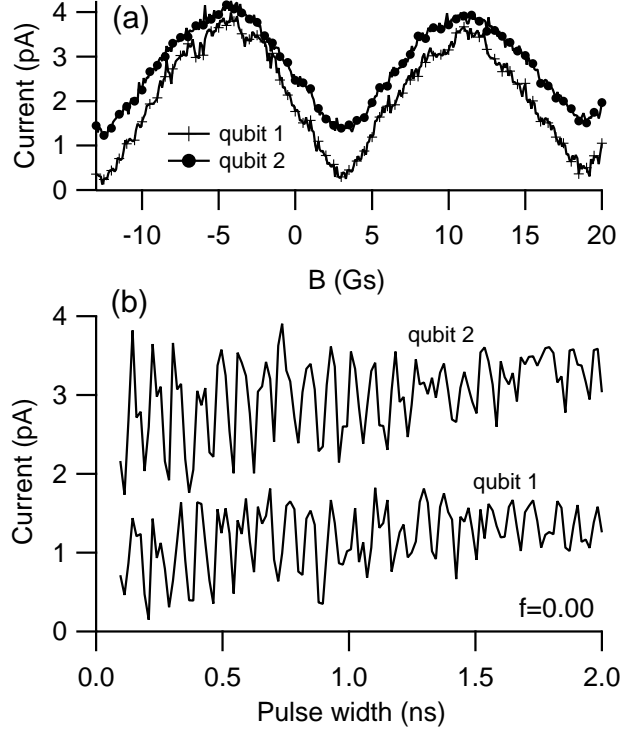


FIG. 2: (a) Magnetic field dependence of the Josephson quasiparticle current through the two probe electrodes in sample A. The currents become maximum not at zero field because of the constant background field. (b) Coherent oscillations of sample A at the flux bias $f=0.00$. Two probe currents are plotted as a function of the duration time of a non-adiabatic voltage pulse applied to the gate electrode. For clarity, the trace for qubit 1 is offset by -0.6 pA.

TABLE I: Parameters of the measured devices. sample E does not have a coupling junction.

Sample	E_{c1}/h (GHz)	$2E_{J1}/h$ (GHz)	E_{c2}/h (GHz)	$2E_{J2}/h$ (GHz)	C_0 (fF)	C_s (fF)	E_{c0}/h (GHz)	E_{J0}/h (GHz)	ν_p (GHz)
A	114	11.4	108	11.4	1.7	6.8	8.8	23	20
B	137	13.6	127	12.8	2.0	6.8	8.5	36	25
C	107	17.0	98	16.0	1.7	6.8	8.8	36	25
D	111	23.0	108	23.0	1.6	6.8	8.8	40	27
E	63.6	21.7	66.4	21.6	-	-	-	-	-

irradiation, besides the main JQP peak at $n_{g2} = 0.50$, a small peak on the slope of the JQP peak is observed, which is due to the photon-assisted JQP (PAJQP) cycle.⁴⁹ The peak indicates that the energy of the microwave photon matches the energy gap of the system at the corresponding n_{g2} . While PAJQP peaks on the left-hand side of the JQP peak correspond to a photon-absorption process, we could, in principle, observe PAJQP peaks on the right-hand side of the JQP peak as well, which correspond to a photon-emission process. In fact, we did observe them in some of the samples, but PAJQP peaks on the emission side were much weaker than those on the absorption side, as reported previously.⁴⁹ In the present paper, we focus on PAJQP peaks on the absorption side.

As shown in the inset of Fig. 3, n_{g1} and n_{g2} are swept simultaneously, keeping the relation $n_{g2} = \alpha n_{g1} + \beta$, where α and β are constants. We fixed α to be almost equal to 1, but β could vary due to background charge jumps. Cross capacitances, such as a capacitance between “box 1” and the “dc gate 2”, are taken into account when we determine the relation between n_{g1} and n_{g2} from the relation between V_{g1} and V_{g2} .

In the current through probe 1 (I_1), we observed similar PAJQP peaks. Thus, we obtained the peak positions n_{g1}^0 and n_{g2}^0 at a particular microwave frequency ν from the I_1 and the I_2 traces, respectively. We repeated this measurement for different values of ν and f .

In Fig. 4 we plot n_{g2}^0 as a function of ν when (a) $f=0.00$, (b) $f=0.25$, and (c) $f=0.37$. The step in ν is 0.1 GHz. The peaks observed at $n_{g2} = 0.50$, independently of the microwave frequency, are the main JQP peaks. We

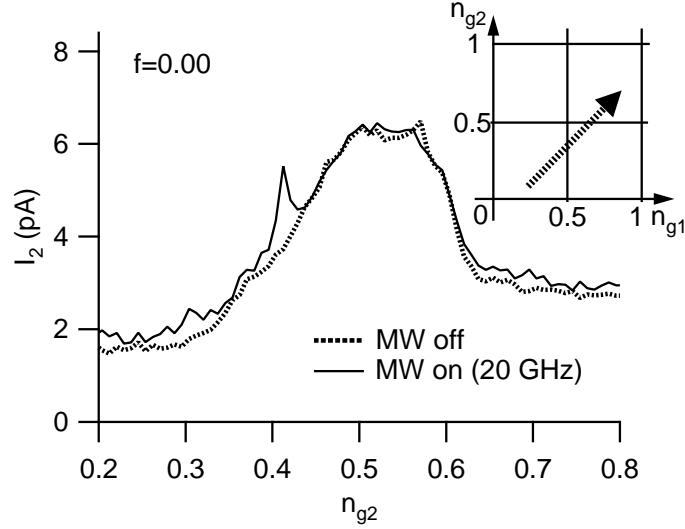


FIG. 3: An example of the spectroscopic measurements. The current through probe electrode 2 is plotted as a function of n_{g2} , the normalized gate-induced charge on the gate electrode 2. The dotted curve is the data when no microwave is applied, while the solid curve is the one when a 20 GHz microwave is applied. The inset shows the direction of the gate sweep in the (n_{g1}, n_{g2}) plane.

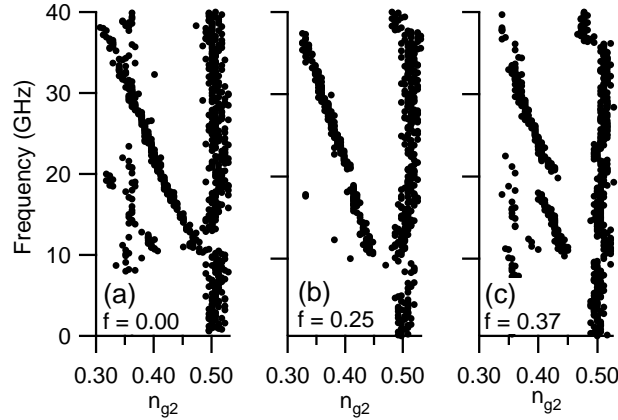


FIG. 4: Results of the spectroscopic measurement for qubit 2 of sample A under the flux bias (a) $f=0.00$, (b) $f=0.25$, and (c) $f=0.37$. The black dots represent the positions of the photon-assisted Josephson quasiparticle peaks at the corresponding frequencies of the applied microwave.

sometimes observe gate-independent peaks at $n_{gi} \neq 0.50$ (such as those at $n_{g2} \sim 0.35$ in Fig. 4(a)), which maybe due to spurious resonant modes in the surrounding circuit. On the left-hand side of the main JQP peaks, frequency-dependent branches are observed. When $f = 0.00$, this branch is continuous and crosses $n_{g2} = 0.50$ at $2E_{J2}/h$. The overall feature looks similar to that observed in a single qubit.⁴⁹ When $f = 0.25$, a small gap appears in the frequency-dependent branch at around $\nu = 20$ GHz. As we increase f further ($f = 0.37$), the gap grows in size, becoming a clear anticrossing. We also observe a similar behavior in I_1 , as shown later. This anticrossing is the manifestation of the *coupling* between the corresponding qubit and the plasma mode of the coupling junction. When $f = 0.00$, the circulating current is zero, hence there is no coupling between them. As f is increased, a circulating current develops, which gives rise to the coupling. This is the essence of the controllable coupling scheme in Ref. 28. We note that this anticrossing was never observed at any f in the sample E, which had *no* coupling junction, supporting the validity of this intuitive picture. In the next section, we analyze the data in a more quantitative way.

III. DISCUSSION

A. Energy-band calculations

In order to further analyze the results of the spectroscopic experiments, we calculated the energy spectrum of the system. Because Eq. (2) may not be a good approximation for our relatively small E_{J0}/E_{Ji} ratio, we started from Eq. (1). Here we use a method similar to the one discussed in Ref. 50. By considering the wave function $\Psi(\phi) = \exp(i\mathbf{k}' \cdot \phi)\chi(\phi)$, where $\mathbf{k}' = [n_{g1}, n_{g2}, -(n_{g1} + n_{g2})]$ and $\phi = (\phi_{p1}, \phi_{p2}, \phi_0/2)$, we obtain a simpler Hamiltonian for $\chi(\phi)$,

$$H_0 = \sum_{i=1}^2 -E_{ci} \frac{\partial^2}{\partial \phi_{pi}^2} - 2E_{J1} \cos \phi_{p1} \cos\left(\pi f + \frac{\phi_0}{2}\right) - 2E_{J2} \cos \phi_{p2} \cos\left(\pi f - \frac{\phi_0}{2}\right) - E_{c0} \frac{\partial^2}{\partial \phi_0^2} - E_{J0} \cos \phi_0. \quad (6)$$

Here we also used the relation $n_i = -i \frac{\partial}{\partial \phi_{pi}}$ and $n_0 = -i \frac{\partial}{\partial \phi_0}$. Because the Josephson-energy terms are periodic with respect to ϕ , the eigenfunctions of the Hamiltonian should be of the Bloch-wave form

$$\chi(\phi) = u_{\mathbf{k}}(\phi) \exp(i\mathbf{k} \cdot \phi), \quad (7)$$

where $\mathbf{k} = (k_{p1}, k_{p2}, 2k_0)$ is the quasi-wavenumber. The eigenvalues of the Hamiltonian are obtained as a function of \mathbf{k} , and \mathbf{k} is related to the normalized gate-induced charges by the periodic boundary condition $\Psi(\phi) = \Psi(\phi + 2\pi)$, namely, $n_{g1} + k_{p1} = m_1$, $n_{g2} + k_{p2} = m_2$, and $2k_0 - n_{g1} - n_{g2} = 2m_0$, where m_i 's are integers. We solved the central equation⁵¹ using 1331 reciprocal lattice points.

Figure 5 shows the energy spectrum of Hamiltonian (6) under the flux bias (a) $f=0.00$ and (b) $f=0.37$. The sample parameters were taken from Table I (sample A). For the gate charges, $n_{g2} = (1.0 n_{g1} - 0.11)$ was assumed for $f=0.00$, and $n_{g2} = (1.0 n_{g1} - 0.21)$ for $f=0.37$, which are the experimental conditions used in Fig. 4.

Roughly speaking, the energy bands consist of those of two qubits with different “photon” numbers for the oscillator of the coupling junction. For example, the energy bands of the two qubits with the coupling junction in the ground state (zero-photon state) are shown in thin red lines in Fig. 5(b). The energy gap between the ground state and the first excited state at the charge degeneracy point, namely, at $n_{g1} (n_{g2}) = 0.5$ for qubit 1 (2) is equal to $2E_{J1} \cos \pi f$ ($2E_{J2} \cos \pi f$). Besides these anticrossings at the charge degeneracy point, there are additional anticrossings at the positions indicated by the arrows, where the energy bands for the zero-photon state cross with those for the one-photon state. Actually, the anticrossings marked by the dotted red arrows are observed in the experiment. The left one corresponds to the anticrossing at $n_{g1} \simeq 0.42$ in Fig. 6(c) and the right one corresponds to the anticrossing at $n_{g2} \simeq 0.42$ in Fig. 6(d). These anticrossings are the manifestation of the coupling between the corresponding qubit and the coupling junction. The anticrossings disappear at $f=0.00$, as seen in Fig. 5(a), where we expect no coupling.

There is one more anticrossing at the point indicated by the dotted circle in Fig. 5(b), where the two energy bands with zero-photon state cross with each other. This anticrossing is the manifestation of the coupling between two qubits via the coupling junction, but its size is so small that it is hard to resolve in our spectroscopic measurements.

Now we consider the microwave excitation from the ground state. In order for the excitation to a particular excited state to be observed in our readout scheme, that is, to be observed as an extra probe current due to a PAJQP cycle, the transition-matrix element between that state and the ground state must be large enough. In addition, there must be a large enough difference in the expectation value of the charge number for those states. In our calculations, we set certain thresholds for these conditions. In Fig. 6, we plot the frequency of the transitions which satisfy the above conditions as a function of n_{g1} (left panels) and n_{g2} (right panels), and compare with the experimental data (for qubit 2, the same data as in Figs. 4(a) and (c)).

The overall agreement is good, considering that all the parameters used for the calculation are determined from *independent* measurements. As we discussed above, the anticrossings observed at $n_{g1,2} \simeq 0.42$ in Figs. 6(c) and (d) are the manifestation of the coupling between the corresponding qubit and the coupling junction, which can be controlled by f . In sample A, we observe split JQP peaks. It seems that these are two overlapping JQP peaks, which may be due to two-level charge fluctuators. This produces two parallel PAJQP branches as seen in Figs. 6(a) and (c).

We investigated the field dependence of the anticrossing further. From the data shown in Fig. 4(c), for example, we extracted the center frequency (ν_0) and the minimum energy gap ($\delta\nu$) of the anticrossing. We analyzed the data at various f 's and plotted ν_0 and $\delta\nu$ as a function of f in Fig. 7. Because the data for qubit 1 was rather noisy and it was difficult to extract $\delta\nu$ and ν_0 , only the data for qubit 2 is used for this plot. The dotted lines are the theoretical prediction from the band calculations and they reproduce well the overall trend of the experimental data. The disagreement in the absolute value for the center frequency is probably due to the error in E_{c0} and E_{J0} , which are estimated from the area measurements by taking scanning electron micrographs.

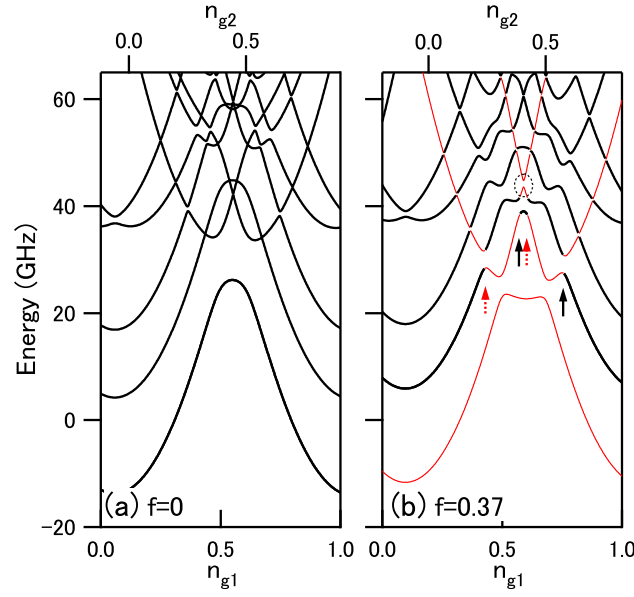


FIG. 5: (color online) (a) Energy spectrum of the coupled-qubit system for $f=0$ and $n_{g2} = (1.0n_{g1} - 0.11)$. (b) Energy spectrum of the coupled-qubit system for $f=0.37$ and $n_{g2} = (1.0n_{g1} - 0.21)$. The energy bands with zero-photon state for the plasma mode of the coupling junction are shown in thin red lines. Four arrows indicate the positions where anticrossings, due to the coupling between one of the two qubits and the plasma mode of the coupling junction, are observed. Two of them shown in dotted red lines correspond to the anticrossings observed in the experiment. A small dotted circle shows the anticrossing due to the coupling between the qubits, via the coupling junction.

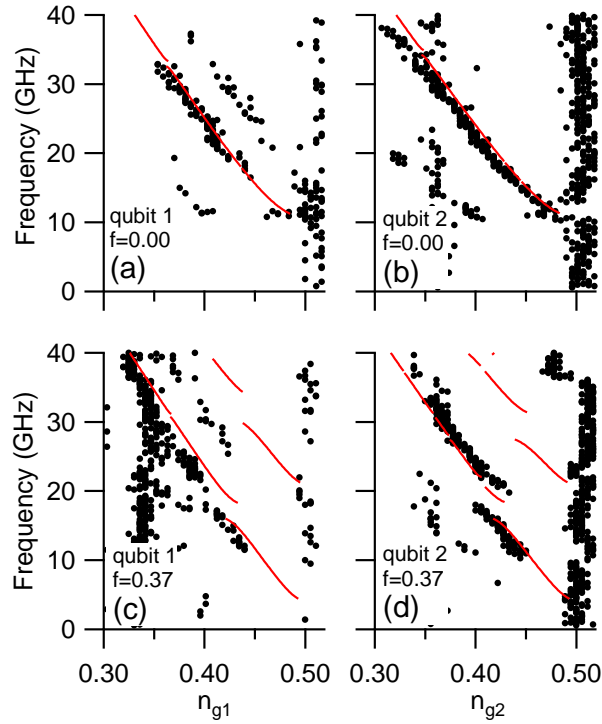


FIG. 6: (color online) Comparison between the theory and the experimental data from the spectroscopic measurements. Black dots are the experimentally-obtained positions of photon-assisted Josephson quasiparticle peaks, and the red solid lines are the results of energy-band calculations.

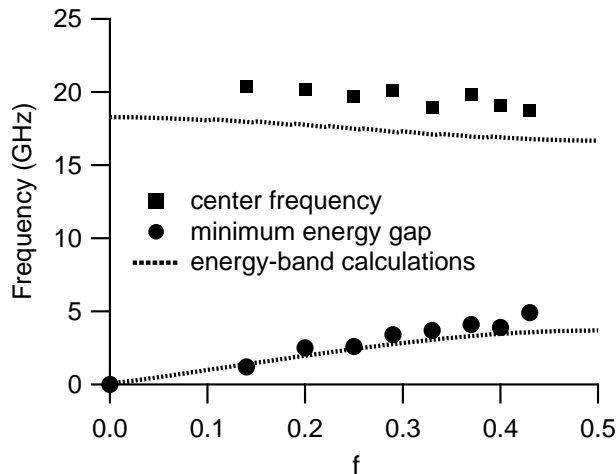


FIG. 7: Observed “center frequency” and minimum energy gap of the anticrossing as a function of the reduced flux bias f . Only the data for qubit 2 is used. The dotted lines show the theoretical predictions from energy-band calculations.

Although we demonstrated the controllable coupling between the coupling junction and one of the two qubits, the final goal is to demonstrate the controllable coupling between the qubits. One demonstration would be time-domain experiments similar to those in Ref. 12. When both qubits are brought to the charge degeneracy point at the same time, by applying a non-adiabatic voltage pulse to the gate electrode, the probe currents as a function of pulse width are expected to show beatings. In an ideal situation, namely, with a pure $|00\rangle$ as an initial state, with an infinitesimal rise/fall time of a non-adiabatic pulse, and with no decoherence, the induced probe current I_i under the effective Hamiltonian (2) is proportional to $1 - \cos(2\chi\Delta t/\hbar)\cos(2E_{Ji}\Delta t/\hbar)$, where $i=1, 2$, and Δt is the pulse width. From this formula the strength of the coupling χ can be detected as the envelope of the oscillations of the probe current. We checked in the calculation that the beating also occurs when we use the Hamiltonian (1).

We tried this idea in the experiments. We could observe the change of the oscillation frequency by applying an external magnetic field, but could not observe a clear change of the envelope in any of the samples listed in Table I. This is probably because of decoherence and the finite rise/fall time of the non-adiabatic voltage pulse, the latter of which reduces the contrast of the beatings. It would be interesting to test the present coupling scheme using qubits with much higher E_J/E_c ratio, like the qubits used in Ref. 6, with a microwave pulse instead of a non-adiabatic pulse for qubit driving.

IV. CONCLUSION

We studied the spectroscopy of two charge qubits coupled by a Josephson inductance under various flux biases. The overall spectrum agrees well with the theory. We observed the anticrossings, which are the manifestation of the coupling between the coupling junction and one of the two qubits. The size of the anticrossing depends on the magnetic flux and disappears at zero flux, demonstrating that the coupling is controllable.

ACKNOWLEDGEMENTS

The authors would like to thank Y. Makhlin, M. Wallquist, V. Shumeiko and G. Wendin for fruitful discussions, and S. Ashhab for valuable comments on the manuscript. This work was partially supported by Japan Science and Technology Agency. F.N. was supported in part by the U.S. National Security Agency (NSA), Army Research Office (ARO), Laboratory of Physical Sciences (LPS), the National Science Foundation Grant No. EIA-0130383, and a JSPS CTC program. J.Q.Y. was supported in part by the National Natural Science Foundation of China grant Nos.

10474013 and 10534060, and the NFRPC grant No. 2006CB921205.

-
- * on leave from Lebedev Physical Institute, Moscow 119991, Russia
- ¹ Y. Makhlin, G. Schön, and A. Shnirman, *Rev. Mod. Phys.* **73**, 357 (2001).
 - ² M. H. Devoret and J. M. Martinis, in *Quantum entanglement and information processing*, edited by D. Esteve, J.-M. Raimond, and J. Dalibard (Elsevier Science, 2005), chap. 12.
 - ³ J. Q. You and F. Nori, *Phys. Today* **58**, No. 11, 42 (2005).
 - ⁴ G. Wendin and V. S. Shumeiko, in *Handbook of Theoretical and Computational Nanotechnology vol. 3*, edited by M. Rieth and W. Schommers (American Scientific Publishers, 2006), p. 223.
 - ⁵ Y. Nakamura, Yu. A. Pashkin, and J. S. Tsai, *Nature* **398**, 786 (1999).
 - ⁶ D. Vion, A. Aassime, A. Cottet, P. Joyez, H. Pothier, C. Urbina, D. Esteve, and M. H. Devoret, *Science* **296**, 887 (2002).
 - ⁷ O. Astafiev, Yu. A. Pashkin, Y. Nakamura, T. Yamamoto, and J. S. Tsai, *Phys. Rev. Lett.* **93**, 267007 (2004).
 - ⁸ G. Ithier, E. Collin, P. Joyez, P. J. Meeson, D. Vion, D. Esteve, F. Chiarello, A. Shnirman, Y. Makhlin, J. Schrieffer, and G. Schön, *Phys. Rev. B* **72**, 134519 (2005).
 - ⁹ P. Bertet, I. Chiorescu, G. Burkard, K. Semba, C. J. P. M. Harmans, D. P. DiVincenzo, and J. E. Mooij, *Phys. Rev. Lett.* **95**, 257002 (2005).
 - ¹⁰ F. Yoshihara, K. Harrabi, A. O. Niskanen, Y. Nakamura, and J. S. Tsai, *Phys. Rev. Lett.* **97**, 167001 (2006).
 - ¹¹ K. Kakuyanagi, T. Meno, S. Saito, H. Nakano, K. Semba, H. Takayanagi, F. Deppe, and A. Shnirman, *Phys. Rev. Lett.* **98**, 047004 (2007).
 - ¹² Yu. A. Pashkin, T. Yamamoto, O. Astafiev, Y. Nakamura, D. V. Averin, and J. S. Tsai, *Nature* **421**, 823 (2003).
 - ¹³ A. J. Berkley, H. Xu, R. C. Ramos, M. A. Gubrud, F. W. Strauch, P. R. Johnson, J. R. Anderson, A. J. Dragt, C. J. Lobb, and F. C. Wellstood, *Science* **300**, 1548 (2003).
 - ¹⁴ T. Yamamoto, Yu. A. Pashkin, O. Astafiev, Y. Nakamura, and J. S. Tsai, *Nature* **425**, 941 (2003).
 - ¹⁵ J. B. Majer, F. G. Paauw, A. C. J. ter Haar, C. J. P. M. Harmans, and J. E. Mooij, *Phys. Rev. Lett.* **94**, 090501 (2005).
 - ¹⁶ R. McDermott, R. W. Simmonds, M. Steffen, K. B. Cooper, K. Cicak, K. D. Osborn, S. Oh, D. P. Pappas, and J. M. Martinis, *Science* **307**, 1299 (2005).
 - ¹⁷ M. Grajcar, A. Izmalkov, S. H. W. van der Ploeg, S. Linzen, T. Plecenik, T. Wagner, U. Hübner, E. Il'ichev, H.-G. Meyer, A. Y. Smirnov, P. J. Love, A. Maassen van den Brink, M. H. S. Amin, S. Uchaikin, and A. M. Zagoskin, *Phys. Rev. Lett.* **96**, 047006 (2006).
 - ¹⁸ M. Steffen, M. Ansmann, R. C. Bialczak, N. Katz, E. L. R. McDermott, M. Neeley, E. M. Weig, A. N. Cleland, and J. M. Martinis, *Science* **313**, 1423 (2006).
 - ¹⁹ J. H. Plantenberg, P. C. de Groot, C. J. P. M. Harmans, and J. E. Mooij, *Nature* **447**, 836 (2007).
 - ²⁰ T. Hime, P. A. Reichardt, B. L. T. Plourde, T. L. Robertson, C.-E. Wu, A. V. Ustinov, and J. Clarke, *Science* **314**, 1427 (2006).
 - ²¹ S. H. W. van der Ploeg, A. Izmalkov, A. Maassen van den Brink, U. Hübner, M. Grajcar, E. Il'ichev, H.-G. Meyer, and A. M. Zagoskin, *Phys. Rev. Lett.* **98**, 057004 (2007).
 - ²² R. Harris, A. J. Berkley, M. W. Johnson, P. Bunyk, S. Govorkov, M. C. Thom, S. Uchaikin, A. B. Wilson, J. Chung, E. Holtham, J. D. Biamonte, A. Yu. Smirnov, M. H. S. Amin, and A. Maassen van den Brink, *Phys. Rev. Lett.* **98**, 177001 (2007).
 - ²³ A. O. Niskanen, K. Harrabi, F. Yoshihara, Y. Nakamura, S. Lloyd, and J. S. Tsai, *Science* **316**, 723 (2007).
 - ²⁴ J. Majer, J. M. Chow, J. M. Gambetta, J. Koch, B. R. Johnson, J. A. Schreier, L. Frunzio, D. I. Schuster, A. A. Houck, A. Wallraff, A. Blais, M. H. Devoret, S. M. Girvin, and R. J. Schoelkopf, *Nature* **449**, 443 (2007).
 - ²⁵ M. A. Sillanpää, J. I. Park, and R. W. Simmonds, *Nature* **449**, 438 (2007).
 - ²⁶ Y. Makhlin, G. Schön, and A. Shnirman, *Nature* **398**, 305 (1999).
 - ²⁷ J. Q. You, J. S. Tsai, and F. Nori, *Phys. Rev. Lett.* **89**, 197902 (2002).
 - ²⁸ J. Q. You, J. S. Tsai, and F. Nori, *Phys. Rev. B* **68**, 024510 (2003).
 - ²⁹ D. V. Averin and C. Bruder, *Phys. Rev. Lett.* **91**, 057003 (2003).
 - ³⁰ B. L. T. Plourde, J. Zhang, K. B. Whaley, F. K. Wilhelm, T. L. Robertson, T. Hime, S. Linzen, P. A. Reichardt, C.-E. Wu, and J. Clarke, *Phys. Rev. B* **70**, 140501(R) (2004).
 - ³¹ J. Lantz, M. Wallquist, V. S. Shumeiko, and G. Wendin, *Phys. Rev. B* **70**, 140507(R) (2004).
 - ³² C. Rigetti, A. Blais, and M. Devoret, *Phys. Rev. Lett.* **94**, 240502 (2005).
 - ³³ M. Wallquist, J. Lantz, V. S. Shumeiko, and G. Wendin, *New J. Phys.* **7**, 178 (2005).
 - ³⁴ A. Maassen van den Brink, A. J. Berkley, and M. Yalowsky, *New J. Phys.* **7**, 230 (2005).
 - ³⁵ P. Bertet, C. J. P. M. Harmans, and J. E. Mooij, *Phys. Rev. B* **73**, 064512 (2006).
 - ³⁶ Y. -X Liu, L. F. Wei, J. S. Tsai, and F. Nori, *Phys. Rev. Lett.* **96**, 067003 (2006).
 - ³⁷ A. O. Niskanen, Y. Nakamura, and J. S. Tsai, *Phys. Rev. B* **73**, 094506 (2006).
 - ³⁸ G. S. Paraoanu, *Phys. Rev. B* **74**, 140504(R) (2006).
 - ³⁹ S. Ashhab, S. Matsuo, N. Hatakenaka, and F. Nori, *Phys. Rev. B* **74**, 184504 (2006).
 - ⁴⁰ M. Grajcar, Y. -X Liu, F. Nori, and A. M. Zagoskin, *Phys. Rev. B* **74**, 172505 (2006).
 - ⁴¹ S. Ashhab and F. Nori, *Phys. Rev. B* **76**, 132513 (2007).

- ⁴² Y. -X Liu, L. F. Wei, J. R. Johansson, J. S. Tsai, and F. Nori, Phys. Rev. B **76**, 144518 (2007).
- ⁴³ S. Ashhab, A. O. Niskanen, K. Harrabi, Y. Nakamura, T. Picot, P. C. de Groot, C. J. P. M. Harmans, J. E. Mooij, and F. Nori, cond-mat/0709.0237.
- ⁴⁴ S. R. Hartmann and E. L. Hahn, Phys. Rev. **128**, 2042 (1962).
- ⁴⁵ M. H. S. Amin, Phys. Rev. B **71**, 024504 (2005).
- ⁴⁶ C. Hutter, Y. Makhlin, A. Shnirman, and G. Schön, Phys. Rev. B **76**, 024512 (2007).
- ⁴⁷ J. Q. You, J. S. Tsai, and F. Nori, Phys. Rev. B **73**, 014510 (2006).
- ⁴⁸ T. A. Fulton, P. L. Gammel, D. J. Bishop, L. N. Dunkleberger, and G. J. Dolan, Phys. Rev. Lett. **63**, 1307 (1989).
- ⁴⁹ Y. Nakamura, C. D. Chen, and J. S. Tsai, Phys. Rev. Lett. **79**, 2328 (1997).
- ⁵⁰ T. P. Orlando, J. E. Mooij, L. Tian, C. H. van der Wal, L. S. Levitov, S. Lloyd, and J. J. Mazo, Phys. Rev. B **60**, 15398 (1999).
- ⁵¹ C. Kittel, *Introduction to Solid State Physics*, 8th ed. (Wiley, New York, 2005), chap. 7.